

Microscopic structure and dynamics of a partial bilayer smectic liquid crystal

Yves Lansac, Matthew A. Glaser, and Noel A. Clark

Condensed Matter Laboratory, Department of Physics, and Ferroelectric Liquid Crystal Materials Research Center,
University of Colorado, Boulder, Colorado 80309

(Received 30 April 2001; published 16 October 2001)

Cyanobiphenyls (nCB's) represent a useful and intensively studied class of mesogens. Many of the peculiar properties of nCB's (e.g., the occurrence of the partial bilayer smectic- A_d phase) are thought to be a manifestation of short-range antiparallel association of neighboring molecules, resulting from strong dipole-dipole interactions between cyano groups. To test and extend existing models of microscopic ordering in nCB's, we carry out large-scale atomistic simulation studies of the microscopic structure and dynamics of the Sm- A_d phase of 4-octyl-4'-cyanobiphenyl (8CB). We compute a variety of thermodynamic, structural, and dynamical properties for this material, and make a detailed comparison of our results with experimental measurements in order to validate our molecular model. Semiquantitative agreement with experiment is found: the smectic layer spacing and mass density are well reproduced, translational diffusion constants are similar to experiment, but the orientational ordering of alkyl chains is overestimated. This simulation provides a detailed picture of molecular conformation, smectic layer structure, and intermolecular correlations in Sm- A_d 8CB, and demonstrates that pronounced short-range antiparallel association of molecules arising from dipole-dipole interactions plays a dominant role in determining the molecular-scale structure of 8CB.

DOI: 10.1103/PhysRevE.64.051703

PACS number(s): 61.30.-v, 64.70.Md

I. INTRODUCTION

Liquid crystals (LC's), broadly defined as state of matter intermediate between crystalline solid and isotropic liquid are fascinating materials both from a fundamental and an applied point of view [1]. Due to their rich phase behavior, resulting from the delicate interplay of fluidity and self organization, LC's play an important role in biological systems (for example, lipid membranes) and in technological applications, in particular electro-optic displays (utilizing nematic and, more recently, ferroelectric LC's [2]). Despite its key importance for the synthesis of LC materials having optimal properties for specific technological applications, the relationship of macroscopic properties to molecular structure and microscopic organization is poorly understood. This is mainly due to the extreme sensitivity of the LC properties to small changes in the molecular architecture, itself a consequence of the intricate interplay of a variety of energetic and entropic effects responsible for the spontaneous formation of mesophases.

Due to the rapid growth in available computer power, as well as the development of efficient algorithms, Monte Carlo (MC) and molecular dynamics (MD) simulations of chemically realistic molecular models hold considerable promise for investigating the microphysics of LC's and for illuminating the relationship between molecular architecture and macroscopic behavior. Owing to the technical challenges associated with atomistic simulation of LC's, however, there have been only a relatively limited number of atomistic simulation studies of thermotropic LC's [3–26]. The quality of these studies varies widely, and whether or not specific studies meet the criterion of “chemical realism” is debatable. An early reported atomistic simulation of a thermotropic LC [3] was of total duration 60 ps, far too short a time to equilibrate even a small sample [26]. Subsequent work has focused on

the development of improved molecular models and on the simulation of larger systems over greater spans of time.

The main fundamental obstacle to the quantitative modeling of LC phases is the need for highly accurate models of molecular interactions, due to the sensitivity of LC properties to details of molecular structure. The central aims of this paper are to develop and validate the computational infrastructure for achieving realistic modeling of LC materials, and to test methodologies for deriving suitable interaction potentials for LC's. For this purpose, a well-studied experimental system is needed to check the quantitative predictive capabilities of our approach for specific LC compounds.

The partial bilayer phase (Sm- A_d) of a 4-octyl-4'-cyanobiphenyl (8CB) as been chosen for this study because it is the prototypal partial bilayer smectic. The layer spacing of a partial bilayer smectic is intermediate between that of a monolayer smectic ($d \sim l$, where l is the molecular length) and a bilayer smectic ($d \sim 2l$). The layer spacing is $d = 31.432 \text{ \AA}$ at $T = 24^\circ\text{C}$ [27], which is approximately 1.4 times the fully extended molecular length of 22.1 \AA , and d increases with increasing temperature, in contrast to most monolayer SmA materials. In fact, the Sm- A_d phase of 8CB is the “fruit fly” of smectic LC science, being undoubtedly the most studied smectic phase.

The chemical structure and phase diagram of 8CB is shown in Fig. 1. The most notable feature of the chemical

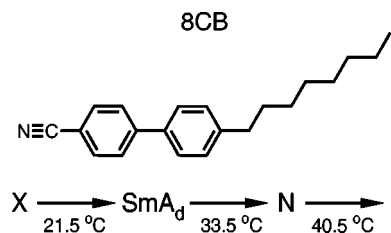


FIG. 1. Chemical structure and phase diagram of 8CB.

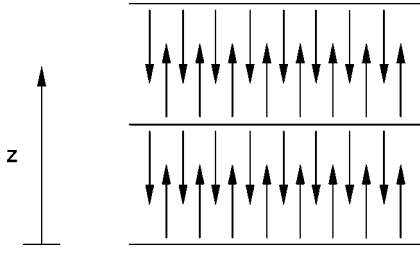


FIG. 2. Schematic representation of the microscopic structure of 8CB, in which each smectic layer consists of two interdigitated polar sublayers. 8CB molecules are depicted as arrows, with the terminal cyano group corresponding to the head of the arrow.

structure of 8CB is the terminal cyano group, which possesses a large dipole moment (4.05 D). The microscopic structure of Sm- A_d 8CB is often represented by cartoons such as that shown in Fig. 2 (see also [28]), in which the smectic layers consist of two well-defined and strongly interdigitated polar sublayers with oppositely oriented terminal dipoles. The substantial interdigitation shown in such cartoons (that leads to $d < 2l$) is thought to be due to dipole-dipole or dipole-induced dipole interactions, which tend to place terminal dipoles next to one another (and antiparallel) or to place terminal dipoles next to the highly polarizable biphenyl group. One objective of this paper is to move our conceptual understanding of the microscopic structure of partial bilayer smectics beyond the cartoon stage. We are particularly interested in learning whether we are capable of modeling 8CB at a sufficient level of physical realism to reproduce the experimental layer spacing. This represents a sensitive test of the interaction potential employed in the simulation, and constitutes a zero-order requirement for quantitative atomistic simulation of smectics.

The paper is organized as follows: In Sec. II, we discuss the methodology of the simulation with a special emphasis on the development of interaction potentials. In Sec. III, we present the results of the large-scale MD simulation of a chemically realistic (atomistic) model of 8CB in the Sm- A_d phase. A direct comparison with experimental measurements on this system is presented, and a detailed picture of the microscopic organization and dynamical properties of 8CB in the smectic phase are developed. In Sec. IV, we summarize our results and discuss future work aimed at more systematic studies of LC behavior.

II. METHODOLOGY

A. Interaction potential

The 8CB molecule is represented by spherically symmetric interaction sites. A hybrid representation is used in which hydrogen atoms in the alkyl tail are absorbed into carbon atoms (methyl and methylene groups are treated as effective atoms) while hydrogen atoms in phenyl rings are kept explicitly in order to reproduce the geometry and charge distribution in a realistic way. This choice is based on the empirical observation that implicit-hydrogen models are able to reproduce many of the thermophysical properties of liquid alkanes

reasonably accurately [29,30] while implicit-hydrogen models for benzene perform poorly [31–33].

Intra- and intermolecular interaction potentials are derived using a combination of *ab initio* and empirical information (for a more detailed review, see [34]). As we are mainly interested in the statistical mechanics of 8CB and not in spectroscopic properties, we choose a simple interaction potential of the form: $U(\mathbf{r}^N) = U_{\text{str}} + U_{\text{bend}} + U_{\text{tors}} + U_{\text{inv}} + U_{\text{vdw}} + U_{\text{coul}}$. The first four terms describe intramolecular interactions, with U_{str} , U_{bend} , U_{tors} , and U_{inv} representing bond stretching, bond-angle bending, dihedral torsion, and “improper” dihedral interactions, respectively. The last two terms describe intermolecular interactions, with U_{vdw} and U_{coul} representing van der Waals and Coulombic interactions, respectively. These contributions to the total potential are defined as

$$U_{\text{str}} = \sum_{\text{bonds } ij} \frac{1}{2} k_r (r_{ij} - r_{\text{eq}})^2, \quad (1)$$

$$U_{\text{bend}} = \sum_{\text{angles } ijk} \frac{1}{2} k_\theta (\theta_{ijk} - \theta_{\text{eq}})^2, \quad (2)$$

$$U_{\text{tors}} = \sum_{\text{dihedrals } ijkl} \sum_{n=0}^6 c_n \phi \cos^n \phi_{ijkl}, \quad (3)$$

$$U_{\text{inv}} = \sum_{\text{umbrellas } ijkl} k_\psi (\cos \psi_{eq} - \cos \psi_{ijkl})^m \quad m = \begin{cases} 1, & \psi_{eq} = 0 \\ 2, & \psi_{eq} \neq 0, \end{cases} \quad (4)$$

$$U_{\text{vdw}} = \sum'_{i < j} 4 \epsilon_{ij} \left[\left(\frac{\sigma_{ij}}{r_{ij}} \right)^{12} - \left(\frac{\sigma_{ij}}{r_{ij}} \right)^6 \right], \quad (5)$$

$$U_{\text{coul}} = \sum'_{i < j} \frac{q_i q_j}{r_{ij}}. \quad (6)$$

The primes on the sums in Eqs. (5) and (6) indicate that 1-2, 1-3, and 1-4 intramolecular nonbonded interactions are excluded from the sums. The internal coordinates r_{ij} , θ_{ijk} , ϕ_{ijkl} , and ψ_{ijkl} are defined by

$$r_{ij} = |\mathbf{r}_{ij}| = |\mathbf{r}_j - \mathbf{r}_i|, \quad (7)$$

$$\theta_{ijk} = \cos^{-1} \left[-\frac{\mathbf{r}_{ij} \cdot \mathbf{r}_{jk}}{r_{ij} r_{jk}} \right], \quad (8)$$

$$\phi_{ijkl} = \cos^{-1} \left[\frac{(\mathbf{r}_{ij} \times \mathbf{r}_{jk}) \cdot (\mathbf{r}_{jk} \times \mathbf{r}_{kl})}{|\mathbf{r}_{ij} \times \mathbf{r}_{jk}| |\mathbf{r}_{jk} \times \mathbf{r}_{kl}|} \right], \quad (9)$$

$$\psi_{ijkl} = \sin^{-1} \left[\frac{\mathbf{r}_{ij} \cdot (\mathbf{r}_{ik} \times \mathbf{r}_{il})}{r_{ij} |\mathbf{r}_{ik} \times \mathbf{r}_{il}|} \right], \quad (10)$$

where r_{ij} is the distance between atomic sites i and j , θ_{ijk} is the angle between bonds ij and jk and ϕ_{ijkl} is the dihedral torsional angle around jk of bonds ij and kl . ψ_{ijkl} measures

TABLE I. Atom types.

Atom type	Description
H_	Hydrogen
C_33	sp^3 carbon with three implicit hydrogens
C_32	sp^3 carbon with two implicit hydrogens
C_R	Resonant carbon (in phenyl)
C_RB	Bridging resonant carbon in biphenyl
C_1	sp^1 carbon
N_1	Nitrogen

the angle between \mathbf{r}_{ij} and the plane defined by \mathbf{r}_{ik} and \mathbf{r}_{il} for three-coordinated atoms i . To retain a symmetric form for the inversion potential, the total inversion potential for a three-coordinated atom i is taken to be the average of three umbrella torsion terms, corresponding to the three possible choices of the unique bond \mathbf{r}_{ij} . Finally, the total rotational potential about a bond is taken to be the sum of potentials for all distinct dihedral angles about the bond, divided by the number of dihedrals. Both of these conventions are borrowed from the Dreiding II force field [35].

The remaining step in building the molecular model is fixing the interaction parameters. These parameters need to be provided for every distinct combination of atom types. We must specify distinct atom types to account for significant variations in geometrical parameters, torsional potentials, etc., among chemically distinct compounds. The atom types used in the present study are given in Table I. The derivation of parameters for 8CB is described in the Appendix.

B. Simulation methodology

We carried out a 8.06 ns *NPT* (constant particle number, constant pressure, and constant temperature) MD simulation of a system containing 100 8CB molecules, at $P=1$ atm and $T=290$ K, followed by a 2 ns *NVT* (constant particle number, constant volume, and constant temperature) MD simulation. Most thermodynamic averages presented below were computed from the 2 ns *NVT* simulation. Note that the simulation is performed at a temperature slightly below the crystal–Sm- A_d transition. Preliminary simulations indicated that the Sm- A_d –N transition temperature for our model is shifted downward with respect to the experimental value (the equilibrium mass density for the simulated system is also lower than the experimental mass density at the same temperature), so we carried out our simulations at a temperature slightly below the Sm- A_d phase range to ensure stable smectic ordering.

We utilize a highly optimized multiple-timestep MD (*r*-RESPA) [36,37] scheme with five distinct intervals of force evaluation, corresponding to bond stretching (0.417 fs), bond-angle bending (0.833 fs), dihedral torsion, and out-of-plane bending (1.667 fs), short-range nonbonded (5 fs) and long-range nonbonded interactions (10 fs). The weak-coupling algorithm of Berendsen *et al.* [38] was used to maintain constant temperature and pressure (for *NPT* MD).

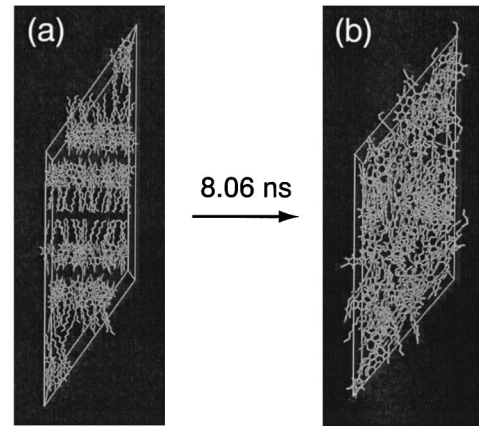


FIG. 3. Initial (a) and final (b) configurations from a 8.06 ns *NPT* MD simulation of 8CB in the Sm- A_d phase.

As mentioned in the previous section, methylene (CH_2) and methyl (CH_3) groups were treated as effective atoms (i.e., single spherically symmetric interaction sites), but full atomic detail is employed otherwise. In particular, hydrogens attached to sp^2 -hybridized carbons in the phenyl rings were included explicitly. However, we set the hydrogen mass equal to that of carbon in this case, to avoid introducing a distinct timestep for fast intramolecular vibrational modes involving hydrogen. This has no effect on the equilibrium distribution, but does modify the dynamics. Specifically, the use of “heavy” hydrogens modifies the intramolecular vibrational spectrum (which is not accurately reproduced by our simple force field in any case) and, more importantly, slightly modifies the overall timescale of the dynamics.

Long-range Coulomb interactions were evaluated to high accuracy using the particle-mesh Ewald (PME) method [39,40], and a standard long-range correction for van der Waals interactions [41] was employed to account for pair interactions beyond the real-space interaction cutoff of 10 Å. The PME technique, which is derived from the conventional Ewald method [42,43], makes use of the fast Fourier transform (FFT) to efficiently compute the long-range part of the electrostatic interaction. The resulting PME algorithm is of order $O(M \log M) \approx O(M)$, where M is the number of charged sites, which must be compared to the optimized Ewald method that scales as $O(M^{3/2})$ [44,45]. We used in this study a highly optimized version of the PME with a relative accuracy of 10^{-4} .

A bilayer (Sm- A_2 -like) initial condition, shown in Fig. 3(a), is used, with perfect polar ordering of 8CB molecules within each half of the bilayer. As can also be seen from this figure, a rather unusual placement of smectic layers within the unit cell is employed, in which each bilayer connects to the adjacent bilayer across the periodic boundaries. Thus, in reality, there is only a single continuous smectic bilayer present in the system. This is done to promote homogeneity of ordering within each distinct smectic sublayer and to minimize finite-size artifacts related to the effective constraint of a constant number of molecules per smectic sublayer (the timescale for permeation of molecules between smectic layers is long compared with the timescale of the

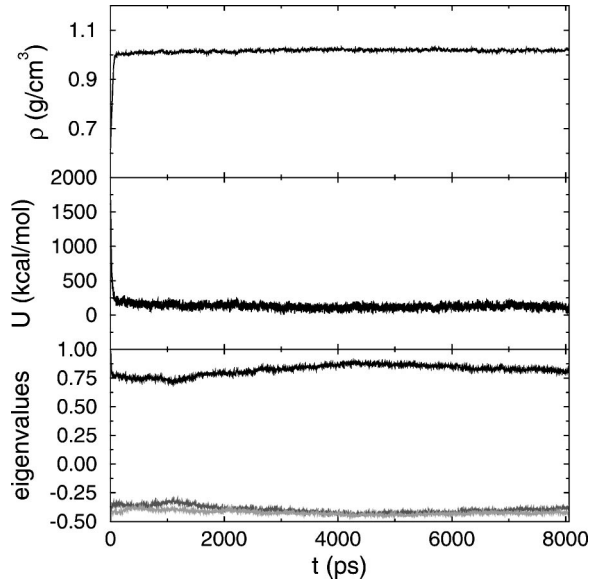


FIG. 4. Time evolution of mass density ρ (a), potential energy U (b), and eigenvalues of the nematic ordering tensor \mathbf{Q} (c), over the duration of an 8.06 ns *NPT* MD simulation of 8CB.

simulation). In this situation, a monoclinic unit cell must be employed if ordinary periodic boundary conditions are used (i.e., if one wishes the cell edge vectors to be Bravais lattice vectors). Alternatively, one could employ an orthorhombic unit cell, with shifted periodic boundary conditions.

III. RESULTS

The final configuration of the *NPT* simulation (after 8.06 ns) is shown in Fig. 3(b). Although smectic layering is still apparent, the organization of the layers is quite complex and fairly disordered, bearing essentially no resemblance to the cartoon of Fig. 2. The essential question is: how faithful a representation of the microscopic organization of the Sm- A_d phase of 8CB is this? To begin to answer this question, we have compared the properties of the simulated system with experiment.

Before doing so, however, we need to verify that the simulated system is equilibrated. In Fig. 4, we have plotted several instantaneous thermodynamic and structural properties as a function of time over the course of the *NPT* simulation. These include the mass density ρ , the potential energy U , and the eigenvalues of the instantaneous nematic ordering tensor \mathbf{Q} . The ordering tensor is defined as

$$Q_{\alpha\beta} = \frac{1}{N} \sum_{i=1}^N \left(\frac{3}{2} u_{i\alpha} u_{i\beta} - \frac{1}{2} \delta_{\alpha\beta} \right), \quad (11)$$

where \mathbf{u}_i is a unit vector coincident with the instantaneous long axis of molecule i (defined as the minimum-moment principal axis of the molecular inertia tensor), $\alpha, \beta = x, y, z$, and the sum ranges over all N molecules. The largest eigenvalue of the ordering tensor defines the nematic order parameter S , and the corresponding eigenvector defines the nematic director \mathbf{n} [46]. All quantities appear to have reached a

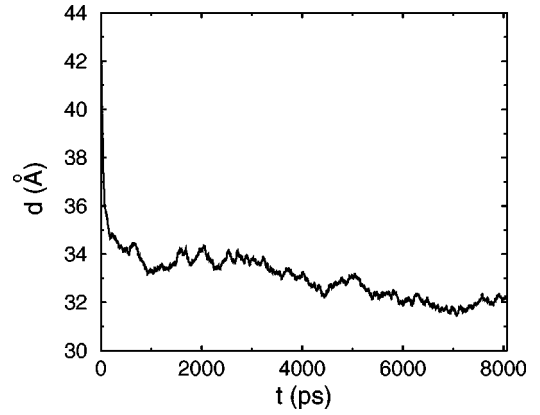


FIG. 5. Time evolution of smectic layer spacing d over the duration of an 8.06 ns *NPT* MD simulation of 8CB.

steady state by the end of the *NPT* simulation, aside from a slight decrease in the nematic order parameter over the last 3 ns of the simulation. The layer spacing d , shown in Fig. 5, shows a more significant long-term variation, although it is approximately constant for the last 2 ns of the *NPT* simulation.

The average layer spacing for the last 2 ns of the *NPT* simulation is $\langle d \rangle = 31.9 \text{ \AA}$, in good agreement with the measured layer spacing of $d_{\text{exp}} = 31.432 \text{ \AA}$ at $T = 24 \text{ }^\circ\text{C}$ [27]. The average simulated mass density, $\rho = 1.018 \text{ g/cm}^3$, is also quite close to the experimental density of $\rho_{\text{exp}} = 1.027 \text{ g/cm}^3$ at $T = 28 \text{ }^\circ\text{C}$ [47].

It is particularly useful to compare the results of the 2 ns *NVT* simulation with experimental measurements that probe the orientational distribution of specific functional groups of 8CB. The average nematic order parameter for the LC core defined as the largest eigenvalue of the tensor $\langle \mathbf{Q}_c \rangle$ (computed using Eq. (11), with \mathbf{u}_i being the long axis of the biphenyl core) gives $S_c = 0.78$, in very good agreement with Raman and optical dichroism measurements, which yield $S_c = 0.77$ at $T = 28 \text{ }^\circ\text{C}$ [48]. We have also made comparisons with deuteron magnetic resonance measurements [49] of the nematic order parameters for C-D bonds in the alkyl tails of partially deuterated 8CB,

$$S_i^{\text{CD}} = \langle P_2(\mathbf{v}_i^{\text{CD}} \cdot \mathbf{z}) \rangle. \quad (12)$$

Here, $P_2(x) = [3 \cos^2(x) - 1]/2$ is the second Legendre polynomial, \mathbf{v}_i^{CD} is a unit vector along a C-D bond connected to the i th carbon in the alkyl tail, and \mathbf{z} is a unit vector normal to the plane of the layers. In Fig. 6, we plot the calculated S_i^{CD} as a function of i , where increasing i corresponds to increasing distance from the core (see insert). As hydrogen atoms in the alkyl tail are not explicitly included in the simulation, we deduce the positions of the hydrogen (or deuterium) atoms from the positions of the backbone carbons, assuming tetrahedral geometry. With the exception of the terminal methyl group, all of the S_i^{CD} are negative, as C-D bonds are approximately perpendicular to the long molecular axis (and thus the layer normal). Also shown in Fig. 6 are the experimental results of Boden *et al.* [49] for two temperatures in the Sm- A_d phase. The simulated order parameters

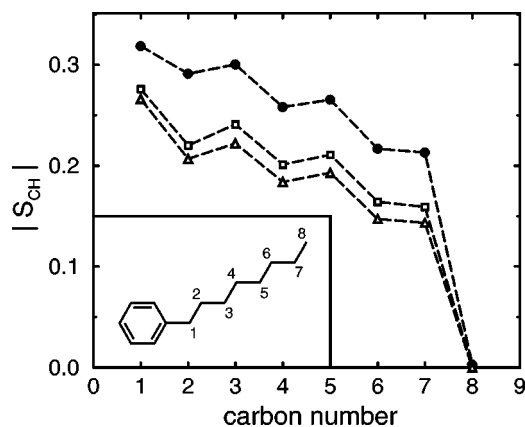


FIG. 6. Order parameters S_i^{CD} as a function of carbon label i for C-D bonds in the alkyl tail of 8CB: ● results from MD simulation ($T=23^\circ\text{C}$); □ NMR measurements at $T=11.5^\circ\text{C}$; △ NMR measurements at $T=21.5^\circ\text{C}$. The labeling of carbon atoms is shown in the inset.

are uniformly larger than these from experiment, although the qualitative trend as a function of i is well reproduced. The discrepancy between simulation and experiment may be due to the small size of the simulated sample (finite-size effects will tend to increase the degree of ordering) or to some inaccuracy in the torsional potentials for the alkyl tail or the tail-core linkage.

The conformations of the flexible alkyl tail can be examined in more detail. The probability that a given rotatable bond in the tail is in the *trans* (planar) configuration rather than one of the *gauche* (bent) states P_j^t is plotted as a function of bond number j in Fig. 7, where bond numbering is defined in the figure insert. There is a pronounced even-odd effect, with a relatively high probability of *gauche* bends (relatively low P_j^t) about even bonds. This may be simply understood by noting that the even-numbered bonds are those that are nearly collinear with the core (at least in the all-*trans* conformation), and *gauche* bends about these bonds result in more-or-less linear molecular configurations, which are not too energetically unfavorable in terms of their steric

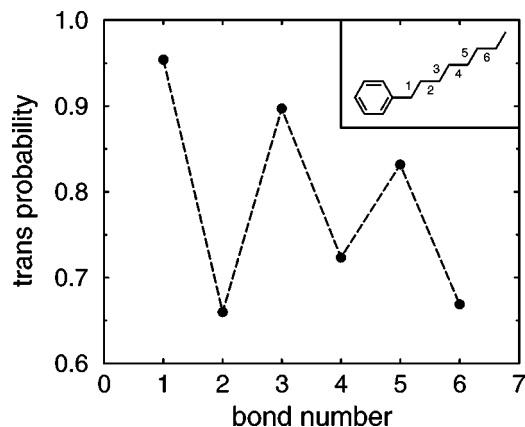


FIG. 7. Probability to find rotatable bonds in the alkyl tail of 8CB in the *trans* (planar) conformation, as a function of bond label (the bond labeling is shown in the inset).

TABLE II. Probabilities of the most populous conformations of the alkyl tail in Sm- A_d 8CB.

Conformation	Probability (%)
<i>ttttt</i>	22.9
<i>tg[±]tttt</i>	10.8
<i>ttttt[±]</i>	10.5
<i>tttg[±]tt</i>	8.0
<i>ttttg[±]t</i>	5.9
<i>tg[±]tttg[±]</i>	3.6
<i>tttg[±]tg[±]</i>	3.5
<i>tg[±]tg[±]tt</i>	3.3
<i>tg[±]tttg[±]</i>	3.1
<i>tttg[±]tg[±]</i>	2.9
<i>tg[±]tg[±]tt</i>	2.3
<i>ttg[±]ttt</i>	2.2
<i>tg[±]ttg[±]t</i>	1.7
<i>tg[±]ttg[±]t</i>	1.4
<i>tg[±]tg[±]tg[±]</i>	1.2
<i>tg[±]tg[±]tg[±]</i>	1.2
<i>ttg[±]tg[±]t</i>	1.1

interactions with surrounding molecules. *Gauche* bends about odd-numbered bonds, on the other hand, lead to strongly bent molecular configurations, which are energetically unfavorable because they fit poorly into the steric cage formed by neighboring molecules. In fact, simple single-molecule mean-field models account well for this even-odd effect (see, for example, [50]).

The most distinctive feature of the data exhibited in Fig. 6 is its “stair-step” appearance. This is a well-studied feature of the aliphatic tails of LC’s materials that can be explained in part with the help of the probability distribution of bond conformation discussed above. If we suppose that the alkyl tail is nearly aligned with the layer normal (i.e., the director of the Sm- A_d phase), it is clear that a *gauche* bond around an even-numbered bond keeps the relative orientation of the C-D bonds sharing the bond mainly unchanged with respect to the director. However a *gauche* bond around an odd-numbered bond changes the orientation (from a plane nearly perpendicular to the director to a plane nearly parallel to the director) of the C-D bonds connected to the even-numbered carbon. As discussed previously, *gauche* bonds about odd-numbered bonds are not very probable but they nevertheless contribute to the overall decrease of the order parameters of the C-D bonds connected to even-numbered carbons. The methyl group (carbon number 8) has a geometry such that one of the three C-D bonds is nearly parallel to the z axis while the other two are nearly perpendicular, so that the overall order parameter computed from the three individual order parameters is very small.

A more detailed picture emerges from an examination of the probability of various conformations of the alkyl tail, listed in Table II. The all-*trans* conformation is the most probable (accounting for nearly 23% of conformations), and conformations having *gauche* bends about even-numbered bonds predominate. Again, the sequence of conformer prob-

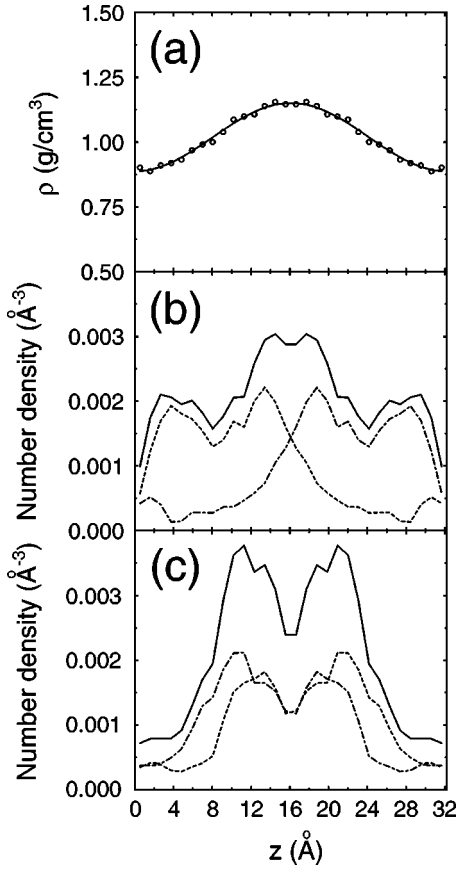


FIG. 8. Mass density profile (a), molecular center of mass number density profile (b), and cyano group number density profile (c) for Sm- A_d 8CB. Also shown in (b) and (c) are the partial number-density profiles for molecules or cyano groups with C \equiv N bonds oriented in the $+z$ direction (dashed curves) and $-z$ direction (dot-dashed curves).

abilities is well accounted for by mean-field theory [50]. The 33 conformations listed account for 85.6% of the total conformations found — 290 distinct conformations account for the other 14.4%.

To characterize the structure of the smectic layers in more detail, we have computed mass and number density profiles along the layer normal \mathbf{z} . These are shown in Fig. 8. The overall mass density profile, shown in Fig. 8(a), is approximately sinusoidal. As we would expect the electron-density profile to be quite similar, it is not surprising that only a single Bragg peak is observed in the x-ray diffraction pattern for 8CB. The molecular center of mass number density profile, shown in Fig. 8(b), is roughly in accord with the notion of a bilayer: molecules with their terminal dipoles directed in the $-z$ direction (dot-dashed curve) are largely confined to the upper half of the layer, while molecules with terminal dipoles pointing in the $+z$ direction (dashed curve) reside mainly in the lower half of the layer. However, there is a significant probability of finding a molecule having a given polarity in the “wrong” half of the layer. The number density profile for cyano groups, shown in Fig. 8(c), indicates that the cyano groups are reasonably well localized in the middle of the layer, with a slight offset of the distribution of

cyano groups with the C \equiv N bond pointing in the $-z$ direction (dot-dashed curve) relative to $+z$ -directed cyano groups. An interesting feature of the overall cyano number density profile is the appearance of two peaks. The origin of this feature is unclear, although it is suggestive that the distance between the two peaks is approximately the length of the biphenyl group.

To shed light on the role of dipole-dipole interactions in determining the structure of the Sm- A_d phase of 8CB, we measured positional and orientational correlation functions for terminal cyano groups. Specifically, we consider the pair-correlation function

$$g^{\text{CN}}(\mathbf{r}) = \frac{1}{\rho N} \left\langle \sum_{i \neq j} \delta(\mathbf{r} - \mathbf{r}_{ij}^{\text{CN}}) \right\rangle \quad (13)$$

and the polar orientational correlation function

$$g_1^{\text{CN}}(\mathbf{r}) = \frac{1}{\rho N g^{\text{CN}}(\mathbf{r})} \left\langle \sum_{i \neq j} P_1(\mathbf{u}_i^{\text{CN}} \cdot \mathbf{u}_j^{\text{CN}}) \delta(\mathbf{r} - \mathbf{r}_{ij}^{\text{CN}}) \right\rangle, \quad (14)$$

where \mathbf{r}_i^{CN} is the position of the center of the i th C \equiv N bond, \mathbf{u}_i^{CN} is a unit vector directed along the i th C \equiv N bond, ρ is the molecular number density, $P_1(x) = \cos(x)$ is the first Legendre polynomial, and the sums range over all pairs of molecules.

In practice, we work either with fully angle-averaged correlation functions, e.g.,

$$g^{\text{CN}}(r) = \frac{1}{4\pi} \int d\Omega g^{\text{CN}}(r, \Omega), \quad (15)$$

or with cylindrically-averaged correlation functions, e.g.,

$$g^{\text{CN}}(r_{\parallel}, r_{\perp}) = \frac{1}{2\pi} \int_0^{2\pi} d\phi g^{\text{CN}}(r_{\parallel}, r_{\perp}, \phi). \quad (16)$$

Here, r_{\parallel} and r_{\perp} denote the components of \mathbf{r} parallel and perpendicular to the reference cyano bond, i.e., $r_{\parallel} = \mathbf{r} \cdot \mathbf{u}^{\text{CN}}$ and $r_{\perp} = |\mathbf{r} - (\mathbf{r} \cdot \mathbf{u}^{\text{CN}}) \mathbf{u}^{\text{CN}}|$, and ϕ is the azimuthal orientation of \mathbf{r} about $\mathbf{u}^{\text{CN}} \times g_1^{\text{CN}}(r)$ and $g_1^{\text{CN}}(r_{\parallel}, r_{\perp})$ are defined in an analogous way.

In Fig. 9 we show the angle-averaged correlation functions $g^{\text{CN}}(r)$ and $g_1^{\text{CN}}(r)$. $g^{\text{CN}}(r)$ [Fig. 9(a)] exhibits a peak at $r = 3.7$ Å, but is otherwise essentially featureless. The prominent negative feature in $g_1^{\text{CN}}(r)$ [Fig. 9(b)] indicates that cyano groups in the first coordination shell surrounding a given cyano are, with a high ($\sim 90\%$) probability, antiparallel to the central cyano group [the minimum value of $g_1^{\text{CN}}(r)$ is less than -0.8 , as compared with the maximum negative value of -1.0].

A more detailed picture emerges when we consider the two-dimensional correlation functions $g^{\text{CN}}(r_{\parallel}, r_{\perp})$ and $g_1^{\text{CN}}(r_{\parallel}, r_{\perp})$, shown in Fig. 10. The reference cyano group is situated at the origin, with the C \equiv N bond directed along the $+r_{\parallel}$ direction [see Fig. 10(c)]. Note that there is a “correlation hole” for $-18 \text{ Å} < r_{\parallel} < 4 \text{ Å}$ and $r_{\perp} < 3 \text{ Å}$ that roughly defines the excluded volume of the central molecule. The

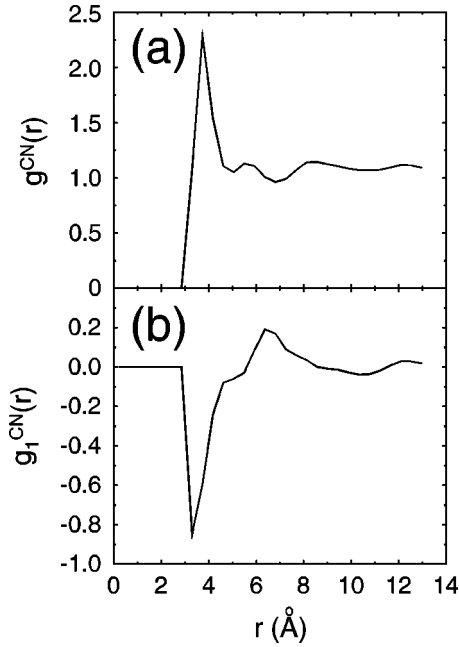


FIG. 9. Angle-averaged pair-correlation function $g^{CN}(r)$ (a) and polar orientational correlation function $g_1^{CN}(r)$ (b) for terminal cyano groups in the Sm- A_d phase of 8CB. The prominent negative feature in $g_1^{CN}(r)$ near $r=3.5$ Å reveals a strong antiparallel correlation of cyano groups in the first coordination shell.

other prominent feature of the data is a ridge of high probability near $r_{\perp}=4$ Å extending from $r_{\parallel}=-15$ Å to $r_{\parallel}=3$ Å. Along this ridge are three peaks, the most prominent of which is at $r_{\parallel}\approx 0.5$ Å, $r_{\perp}\approx 3.5$ Å. This peak reaches a height of six, corresponding to a density of C≡N groups six times their average density. Examination of $g_1^{CN}(r_{\parallel}, r_{\perp})$ [Fig. 10(b)] reveals that the C≡N groups associated with this peak have a strong tendency to be antiparallel to the central C≡N group. Thus, the most significant correlations between cyano groups can be traced to their strong antiparallel association at short distances. The other features of Fig. 10(b) are quite complex, and much more difficult to interpret, but it is clear that the significant correlations do not extend much beyond the first coordination shell.

To study in-layer ordering, we have calculated the in-layer pair-correlation function

$$g(\mathbf{R}) = \frac{1}{\rho N} \left\langle \sum_{i \neq j} \delta(\mathbf{R} - \mathbf{R}_{ij}) \right\rangle, \quad (17)$$

and the in-layer sixfold bond-orientational correlation function

$$g_6(\mathbf{R}) = \frac{1}{\rho N g(\mathbf{R})} \left\langle \sum_{i \neq j} \psi_{6i} \psi_{6j}^* \delta(\mathbf{R} - \mathbf{R}_{ij}) \right\rangle. \quad (18)$$

Here, \mathbf{R}_i is the in-layer position of molecule i , obtained by projecting its center-of-mass position along the long molecular axis into the midplane of the sublayer to which it belongs, and the local bond-orientational order parameter ψ_{6i} is defined as

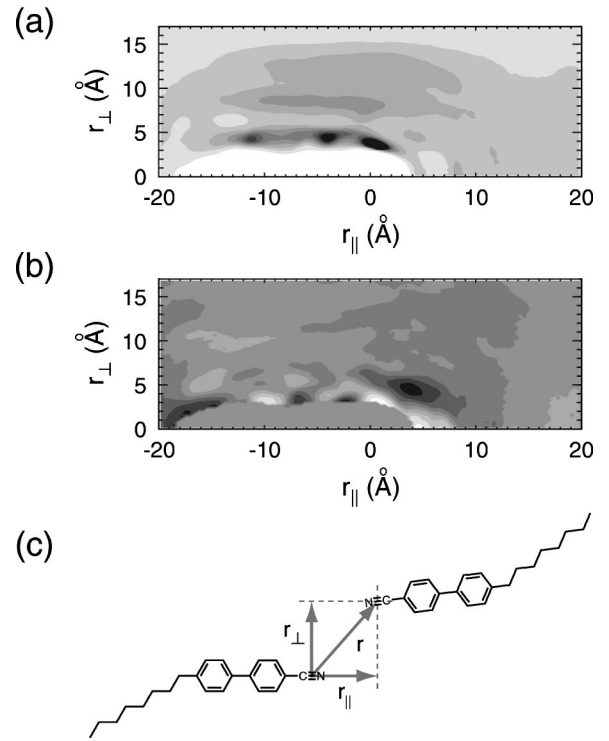


FIG. 10. Two-dimensional pair-correlation function $g^{CN}(r_{\parallel}, r_{\perp})$ (a) and polar orientational correlation function $g_1^{CN}(r_{\parallel}, r_{\perp})$ (b) for terminal cyano groups in the Sm- A_d phase of 8CB. The definition of r_{\parallel} and r_{\perp} is shown schematically in (c).

$$\psi_{6i} = \frac{1}{n_i} \sum_{k=1}^{n_i} e^{i6\theta_{ik}}, \quad (19)$$

where the sum runs over the n_i nearest neighbors of molecule i [51], and θ_{ik} is the orientation of the “bond” between molecules i and k with respect to an arbitrary axis (in this case, the X axis, defined as the axis perpendicular to the layer normal and the unique axis of the monoclinic unit cell). As before, we also compute the angle-averaged correlation functions, e.g.,

$$g(R) = \frac{1}{2\pi} \int_0^{2\pi} g(R, \Theta) d\Theta, \quad (20)$$

where $R=|\mathbf{R}|$, and Θ is the polar orientation of \mathbf{R} in the plane of the layer.

The angle-averaged in-layer correlation functions $g(R)$ and $g_6(R)$ are shown in Fig. 11. The in-layer positional correlations appear to be liquidlike (short ranged), but $g_6(R)$ [Fig. 11(b)] approaches a nonzero constant for large R , which suggests that system possesses some degree of bond-orientational order. A more complete picture of the in-layer structure can be obtained from the full two-dimensional correlation functions $g(X, Y)$ and $g_6(X, Y)$, shown in Fig. 12. These correlation functions exhibit sixfold anisotropy, perhaps due to the fact that the simulated structure is not orthogonal. In fact, we measure a small but finite average tilt angle of $\langle \Theta \rangle = 6.6^\circ$, defined as the angle between the maximum-eigenvalue eigenvector of the average ordering

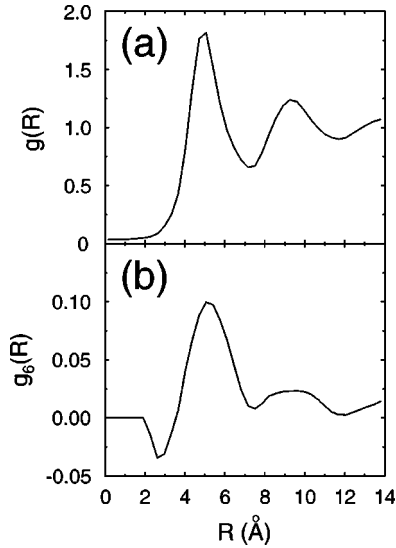


FIG. 11. In-layer angle-averaged pair-correlation function $g(R)$ (a) and bond-orientational correlation function $g_6(R)$ (b).

tensor $\langle \mathbf{Q} \rangle$ and the layer normal \mathbf{z} . Further work will be required to determine whether this is a real feature of the local structure of 8CB.

Finally, we have measured the mean-squared displacement and diffusion constants for 8CB molecules both parallel and perpendicular to the smectic layer normal from the Einstein relations $D = \lim_{t \rightarrow \infty} \langle [\mathbf{r}(t) - \mathbf{r}(0)]^2 \rangle / (6t)$, $D_{\perp} = \lim_{t \rightarrow \infty} \langle [\mathbf{r}_{\perp}(t) - \mathbf{r}_{\perp}(0)]^2 \rangle / (4t)$, and $D_{\parallel} = \lim_{t \rightarrow \infty} \langle [r_{\parallel}(t) - r_{\parallel}(0)]^2 \rangle / (2t)$, where $r_{\parallel}(t)$ is the molecular center-of-mass position at time t projected onto the layer normal, and $\mathbf{r}_{\perp}(t)$ is the molecular center-of-mass position projected into the plane perpendicular to the layer normal.

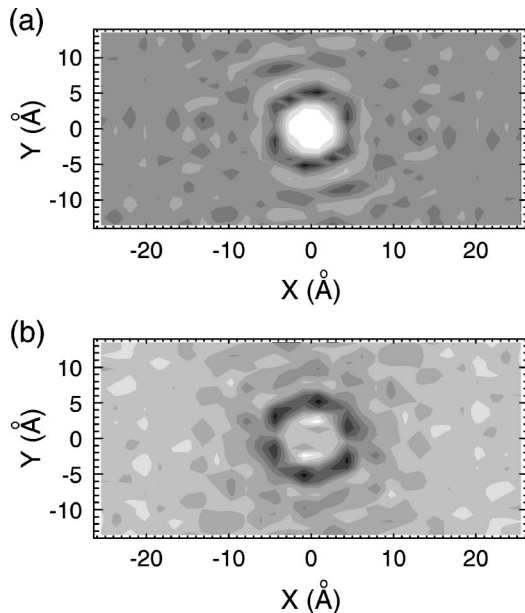


FIG. 12. Two-dimensional in-layer pair-correlation function $g(X, Y)$ (a) and bond-orientational correlation function $g_6(X, Y)$ (b).

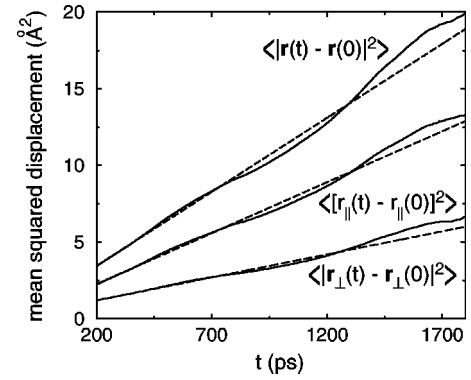


FIG. 13. Mean-square displacement as a function of time for 8CB molecules both parallel ($\langle [r_{\parallel}(t) - r_{\parallel}(0)]^2 \rangle$) and perpendicular ($\langle |\mathbf{r}_{\perp}(t) - \mathbf{r}_{\perp}(0)|^2 \rangle$) to the layer normal. The total mean-square displacement ($\langle |\mathbf{r}(t) - \mathbf{r}(0)|^2 \rangle$) is also shown. The dashed lines are linear fits from which the diffusion constants are derived.

The mean-squared displacement as a function of time is shown in Fig. 13, together with linear fits. The resulting diffusion constants are $D_{\parallel} = 3.32 \times 10^{-7} \text{ cm}^2 \text{ s}^{-1}$ (the diffusion constant parallel to the layer normal), $D_{\perp} = 7.52 \times 10^{-8} \text{ cm}^2 \text{ s}^{-1}$ (the diffusion constant perpendicular to the layer normal), and $D = 1.61 \times 10^{-7} \text{ cm}^2 \text{ s}^{-1}$ (the total diffusion constant). Although we are not aware of measurements of diffusion constants for Sm- A_d 8CB, these diffusion constants are at least of the same order of magnitude as tracer diffusion constants in the nematic phase of 8CB [52]. Notice that D_{\parallel} is larger than D_{\perp} — an interesting question is whether this situation will still hold on timescales long enough that the molecules have diffused a distance comparable to the layer spacing. The effective D_{\parallel} on the permeation timescale may be smaller than the short-time D_{\parallel} , owing to the free-energy barrier encountered by molecules diffusing from layer to layer. The timescale at which this crossover should occur can be estimated from the measured diffusion constants as the time required for molecules to diffuse one layer spacing, ~ 30 Å, corresponding to a mean-squared displacement of ~ 900 Å². Using the measured D_{\parallel} , we estimate that this would take ~ 140 ns. Accessing this dynamical regime will obviously require a substantially greater computational effort.

IV. SUMMARY

We have modeled the Sm- A_d phase of 8CB in a long MD simulation of more than 10 ns. We observe the spontaneous

TABLE III. Van der Waals parameters.

Atom 1	ϵ (kcal/mol)	σ (Å)
H _l	0.030	2.420
C ₃₃	0.226	3.930
C ₃₂	0.093	3.930
C _R	0.070	3.550
C _{RB}	0.070	3.550
C ₁	0.150	3.650
N ₁	0.170	3.200

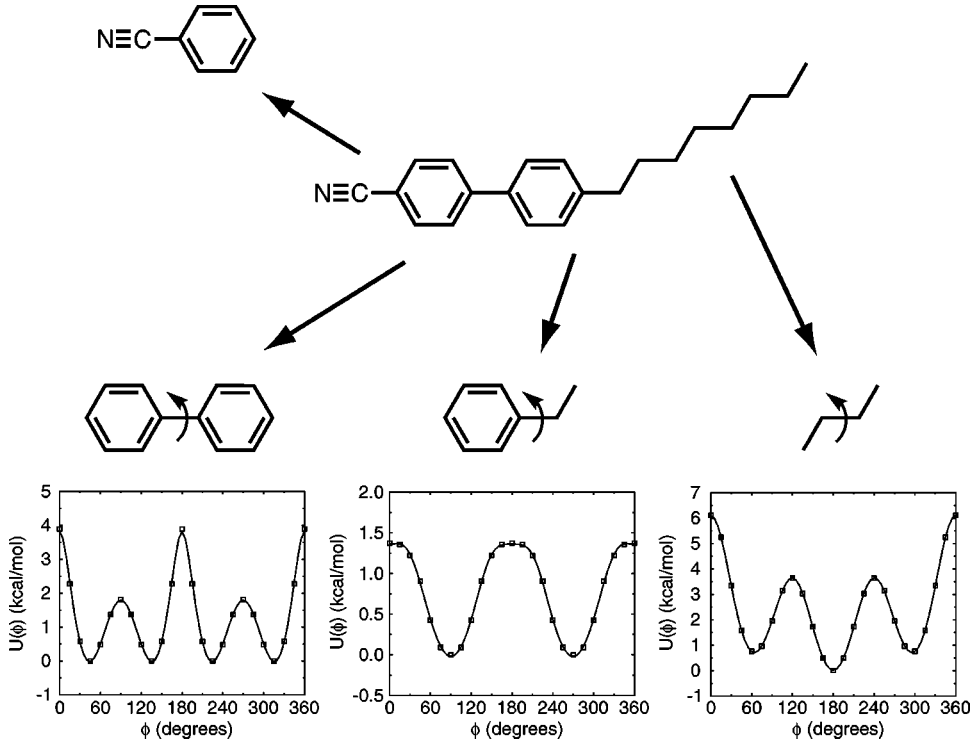


FIG. 14. 8CB molecule with substructures used to parametrize our interaction potential (counterclockwise from top: benzonitrile, biphenyl, ethylbenzene, and butane). Bottom: *ab initio* (symbols) and fitted (solid line) rotational potentials for biphenyl, ethylbenzene, and butane.

formation of the Sm- A_d partial bilayer phase from a bilayer initial condition, with an equilibrium smectic layer spacing close to the experimental value. The equilibrium density, orientational order parameters, and diffusion constants are also in reasonable quantitative agreement with experiment, although the simulated orientational-order parameters for methylene groups in the alkyl tail are systematically higher than those obtained from experiment.

Overall, the results suggest that our model for interatomic interactions in 8CB captures the main physical effects that govern the self organization of cyanobiphenyls (similarly good quantitative agreement with experiment has been found in simulations of other LC materials in which essentially the same methodology for deriving interatomic potentials was employed [26,53]). Specifically, the present study implies that the molecular-scale structure of 8CB is dominated by excluded volume interactions and specific interactions between permanent electric dipoles, with induction effects playing a secondary role [54]. This is physically reasonable,

TABLE IV. Bond-stretching parameters.

Atom 1	Atom 2	r_{eq} (Å)
C_32	C_32	1.53
C_33	C_32	1.53
C_R	C_32	1.51
C_R	C_R	1.39
C_R	H_	1.08
C_RB	C_RB	1.49
C_R	C_RB	1.39
C_R	C_1	1.45
C_1	N_1	1.14

as the dipole-dipole interaction energy for two cyano dipoles (treated as point dipoles with dipole moment 4.05 D) with 3.5 Å separation is $u_{dip}=5.5$ kcal/mol ($u_{dip}/k_B=2770$ K), which is more than a factor of eight larger than the dipole-induced dipole interaction energy for a cyano dipole and a phenyl ring (treated as a point polarizable center with polarizability 10.0 Å³) with 3.5 Å separation, $u_{ind}=0.64$ kcal/mol ($u_{ind}/k_B=320$ K). Moreover, the dipole-dipole interactions are highly directional, while the dipole-induced dipole interactions are more isotropic. For both reasons, one would expect dipole-dipole interactions to play a dominant role in determining short-range intermolecular correlations in cyanobiphenyls.

This study also provides a detailed picture of molecular conformation, intermolecular correlations, and smectic layer structure in Sm- A_d 8CB. In particular, our results show that

TABLE V. Bond-angle-bending parameters.

Atom 1	Atom 2	Atom 3	θ_{eq} (°)
C_32	C_32	C_32	113.1
C_33	C_32	C_32	113.1
C_32	C_32	C_R	112.8
C_32	C_R	C_R	120.0
C_R	C_R	C_R	120.0
C_R	C_R	H_	120.0
C_R	C_R	C_RB	120.0
C_R	C_RB	C_R	120.0
C_R	C_RB	C_RB	120.0
C_RB	C_R	H_	120.0
C_R	C_R	C_1	120.0
C_R	C_1	N_1	180.0

TABLE VI. Torsional parameters (kcal/mol), where X represents any atom.

Atom 1	Atom 2	Atom 3	Atom 4	$c_{0\phi}$	$c_{1\phi}$	$c_{2\phi}$	$c_{3\phi}$	$c_{4\phi}$	$c_{5\phi}$	$c_{6\phi}$
C_33	C_32	C_32	C_32	1.965	-4.634	1.459	6.695	-2.683	0.982	2.315
C_32	C_32	C_32	C_32	1.965	-4.634	1.459	6.695	-2.683	0.982	2.315
C_32	C_32	C_32	C_R	1.965	-4.634	1.459	6.695	-2.683	0.982	2.315
C_32	C_32	C_R	C_R	-0.464	4.387	1.309	-8.342	-1.249	5.024	-0.763
C_R	C_RB	C_RB	C_R	4.930	-18.893	-7.108	16.984	3.981	-9.272	-0.214
X	C_R	C_R	X	25.0	0	-25.0	0	0	0	0
X	C_R	C_RB	X	25.0	0	-25.0	0	0	0	0

the microscopic organization of smectic layers in Sm- A_d 8CB is, not surprisingly, considerably more complex than the simple cartoon representation of Fig. 2 would suggest, although strong antiparallel association of neighboring molecules is observed. The in-layer correlation functions reveal liquidlike structure with weak bond-orientational order, perhaps induced by a small but non-negligible molecular tilt.

Future work will focus on more systematic studies of the cyanobiphenyl LC family. In particular, we plan to compute a wider range of properties of this system (including phase behavior, viscosity, and dielectric constants), and to analyze finite-size and finite-time effects. A longer-term goal is to develop polarizable models for cyanobiphenyls that will enable us to explicitly probe the role of induction interactions in these materials.

ACKNOWLEDGMENT

This work was supported by NSF MRSEC Grant No. DMR 98-09555.

APPENDIX: INTERACTION PARAMETERS

In this appendix, we describe the procedure used to parametrize the interaction potential for 8CB, and list the interaction parameters. We make use of a combination of *ab initio* quantum chemistry and empirical data. The basic procedure we employ has been described previously [34].

The van der Waals dispersion/repulsion parameters σ_{ij} and ϵ_{ij} are empirical parameters, taken from the literature. In the present paper, we make use of parameters from OPLS [55], with united atom parameters for CH_2 and CH_3 taken from Siepmann *et al.* [29]. These parameters have been chosen to reproduce the thermophysical properties of small organic molecules in the liquid state, using MD or MC simu-

lation. Standard geometric combination rules were used to parametrize van der Waals interactions between unlike atoms (i.e. $\epsilon_{ij} = \sqrt{\epsilon_{ii}\epsilon_{jj}}$ and $\sigma_{ij} = \sqrt{\sigma_{ii}\sigma_{jj}}$). The relevant parameters used to describe the intermolecular site interactions are listed in Table III.

As we are not aiming for an interaction potential of spectroscopic accuracy, the bond-stretch and angle-bend spring constants k_r and k_θ are given generic values: $k_r = 700 \text{ kcal mol}^{-1} \text{ \AA}^{-2}$ for single bonds, $k_r = 1050 \text{ kcal mol}^{-1} \text{ \AA}^{-2}$ for resonant bonds, $k_r = 1400 \text{ kcal mol}^{-1} \text{ \AA}^{-2}$ for double bonds, and $k_r = 2800 \text{ kcal mol}^{-1} \text{ \AA}^{-2}$ for triple bonds, while a value $k_\theta = 100 \text{ kcal mol}^{-1} \text{ rad}^{-2}$ is used for all bond angles. These values were taken from the Dreiding II force field [35].

The geometrical parameters r_{eq} and θ_{eq} and the torsional interaction parameters $c_{n\phi}$ are obtained from *ab initio* calculations. LC molecules are generally too large to attack directly using an *ab initio* approach. In order to have results with a reasonable accuracy and computation time, we carry out *ab initio* studies of appropriate substructures of LC molecules, assuming that the interaction parameters derived for the substructures are transferable to the whole LC molecule. The transferability hypothesis neglects any coupling between torsions about two adjacent rotatable bonds other than that arising from intramolecular nonbonded interactions.

The substructures used to obtain equilibrium bond lengths, bond angles, and torsional parameters for the 8CB molecule are shown in Fig. 14. The *ab initio* calculations were done at the MP2/6-31G(d)//RHF/6-31G(d) level of theory, which gives a reasonable quality/cost ratio, using GAUSSIAN 94 [56]. The relevant parameters obtained are displayed in Tables IV, V, and VI, respectively, for bond stretching, bond-angle bending, and dihedral torsion. r_{eq} and θ_{eq} are taken directly from optimized *ab initio* structures. The coefficients $c_{n\phi}$ are obtained from fits to the *ab initio* torsional potentials, shown in Fig. 14. In addition, generic values are used for noncritical torsional parameters $c_{n\phi}$ (for example, for dihedrals in phenyl rings), and planarity of the rings is ensured by including an inversion potential with $\psi_{\text{eq}} = 0$ and $k_\psi = 40 \text{ kcal mol}^{-1} \text{ rad}^{-2}$.

Long-range electrostatic interactions are considered explicitly in our simulations. Site charges for substructures and for 8CB are determined from electrostatic potential (ESP CHELPG [57]) fits of a site-charge model to the electrostatic potential calculated from semiempirical (AM1) charge densities for the 8CB molecule. This is done at this empirical level because a higher-level computation of the site-charge

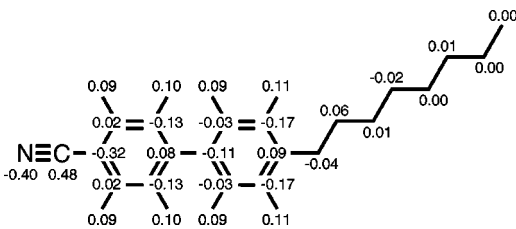


FIG. 15. Site charges (in units of the electron charge) for the 8CB molecule, determined from electrostatic potential (ESP CHELPG [57]) fits to semiempirical (AM1) charge densities.

distribution for the 8CB molecule is too computationally expensive, and because site charges are less transferable than other parameters. Figure 15 lists the values of the site charges used in this study.

It is important to note that in the present simulation, the

induction interactions (the interactions between dipoles induced by the electric field produced by the original charge distribution) are not considered explicitly, but are absorbed into the effective empirical van der Waals parameters ϵ_{ij} and σ_{ij} .

-
- [1] P.G. de Gennes and J. Prost, *The Physics of Liquid Crystals* (Clarendon Press, Oxford, 1993).
- [2] N.A. Clark and S.T. Lagerwall, *Appl. Phys. Lett.* **36**, 899 (1980).
- [3] S.J. Picken, W.F. van Gunsteren, P.Th. van Duijnen, and W.H. de Jeu, *Liq. Cryst.* **6**, 357 (1989).
- [4] A.V. Komolkin, Yu.V. Molchanov, and P.P. Yakutseni, *Liq. Cryst.* **6**, 39 (1989).
- [5] B. Jung and B.L. Schürmann, *Mol. Cryst. Liq. Cryst.* **185**, 141 (1990).
- [6] I. Ono and S. Kondo, *Mol. Cryst. Liq. Cryst., Lett. Sect.* **8**, 69 (1991).
- [7] M.R. Wilson and M.P. Allen, *Mol. Cryst. Liq. Cryst.* **198**, 465 (1991).
- [8] M.R. Wilson and M.P. Allen, *Liq. Cryst.* **12**, 157 (1992).
- [9] A. Maliniak, *J. Chem. Phys.* **96**, 2306 (1992).
- [10] G. Krömer, D. Paschek, and A. Geiger, *Ber. Bunsenges. Phys. Chem.* **97**, 1188 (1993).
- [11] J. Huth, T. Mosell, K. Nicklas, A. Sariban, and J. Brickmann, *J. Phys. Chem.* **98**, 7685 (1994).
- [12] S.Ye. Yakovenko, A.A. Minko, G. Krömer, and A. Geiger, *Liq. Cryst.* **17**, 127 (1994).
- [13] M.A. Glaser, R. Malzbender, N.A. Clark, and D.M. Walba, *J. Phys.: Condens. Matter* **6**, A261 (1994).
- [14] A.V. Komolkin, A. Laaksonen, and A. Maliniak, *J. Chem. Phys.* **101**, 4103 (1994).
- [15] M.A. Glaser, R. Malzbender, N.A. Clark, and D.M. Walba, *Mol. Simul.* **14**, 343 (1995).
- [16] S.Ye. Yakovenko, A.A. Muravski, G. Krömer, and A. Geiger, *Mol. Phys.* **86**, 1099 (1995).
- [17] S.S. Patnaik, S.J. Plimpton, R. Pachter, and W.W. Adams, *Liq. Cryst.* **19**, 213 (1995).
- [18] A.V. Komolkin and A. Maliniak, *Mol. Phys.* **84**, 1227 (1995).
- [19] M.R. Wilson, *J. Mol. Liq.* **68**, 23 (1996).
- [20] D. Sandstroem, A.V. Komolkin, and A. Maliniak, *J. Chem. Phys.* **104**, 9620 (1996).
- [21] D. Sandstroem, A.V. Komolkin, and A. Maliniak, *J. Chem. Phys.* **106**, 7438 (1997).
- [22] S.Y. Yakovenko and A.A. Muravski, *Liq. Cryst.* **24**, 657 (1998).
- [23] C. McBride, M.R. Wilson, and J.A.K. Howard, *Mol. Phys.* **93**, 955 (1998).
- [24] D. Paschek, S.Y. Yakovenko, A.A. Muravski, and A. Geiger, *Ferroelectrics* **212**, 45 (1998).
- [25] Y. Lansac, M.A. Glaser, N.A. Clark, and O.D. Lavrentovich, *Nature (London)* **398**, 54 (1999).
- [26] M.A. Glaser, in *Advances in the Computer Simulations of Liquid Crystals*, edited by C. Zannoni and P. Pasini (Kluwer, Dordrecht, 1999), p. 263.
- [27] T.A. Krentsel, O.D. Lavrentovich, and S. Kumar, *Mol. Cryst. Liq. Cryst. Sci. Technol., Sect. A* **304**, 463 (1997).
- [28] J.L. Lydon and C.J. Coakley, *J. Phys. (France)* **36**, C1-45 (1975); A.J. Leadbetter, R.M. Richardson, and C.N. Colling, *ibid.* **36**, C1-37 (1975).
- [29] J.I. Siepmann, S. Karaborni, and B. Smit, *Nature (London)* **365**, 330 (1993).
- [30] W. Paul, D.Y. Yoon, and G.D. Smith, *J. Chem. Phys.* **103**, 1702 (1995).
- [31] X. Shi and L.S. Bartell, *J. Phys. Chem.* **92**, 5667 (1988).
- [32] L.S. Bartell, L.R. Sharkey, and X. Shi, *J. Am. Chem. Soc.* **110**, 7006 (1988).
- [33] J. Nagy, V.H. Smith, and D.F. Weaver, *J. Phys. Chem.* **99**, 13868 (1995).
- [34] M.A. Glaser, N.A. Clark, E. Garcia, and D.M. Walba, *Spectrochim. Acta, Part A* **53**, 1325 (1997).
- [35] S.L. Mayo, B.D. Olafson, and W.A. Goddard III, *J. Phys. Chem.* **94**, 8897 (1990).
- [36] M. Tuckermann, B.J. Berne, and G.J. Martyna, *J. Phys. Chem.* **97**, 1990 (1992).
- [37] J.C. Sexton and D.H. Weingarten, *Nucl. Phys. B* **380**, 665 (1992).
- [38] H.J.C. Berendsen, J.P.M. Postma, W.F. van Gunsteren, A. Dinola, and J.R. Haak, *J. Phys. Chem.* **81**, 3684 (1984).
- [39] T. Darden, D. York, and L. Pedersen, *J. Phys. Chem.* **98**, 10089 (1993).
- [40] U. Essmann, L. Perera, M.L. Berkowitz, T. Darden, H. Lee, and L.G. Pedersen, *J. Phys. Chem.* **103**, 8577 (1995).
- [41] M.P. Allen and D.J. Tildesley, *Computer Simulation of Liquids* (Oxford University Press, Oxford, 1987).
- [42] P.P. Ewald, *Ann. Phys. (Leipzig)* **64**, 253 (1921).
- [43] For a review of electrostatic methods see A.Y. Toukmaji and J.A. Board Jr., *Comput. Phys. Commun.* **95**, 73 (1996).
- [44] J.W. Perram, H.G. Petersen, and S.W. de Leeuw, *Mol. Phys.* **65**, 875 (1988).
- [45] D. Fincham, *Mol. Sim.* **13**, 1 (1994).
- [46] Alternatively, one could take minus twice the middle eigenvalue of the ordering tensor as the order parameter S [see, R. Eppenga and D. Frenkel, *Mol. Phys.* **52**, 1303 (1984)].
- [47] A.J. Leadbetter, J.L.A. Durrant, and M. Rugman, *Mol. Cryst. Liq. Cryst. Lett.* **34**, 231 (1977).
- [48] S. Kobinata, T. Kobayashi, H. Yoshida, A.D.L. Chandani, and S. Maeda, *J. Mol. Struct.* **146**, 373 (1986).
- [49] N. Boden, L.D. Clark, R.J. Bushby, J.W. Emsley, G.R. Luckhurst, and C.P. Stockley, *Mol. Phys.* **42**, 565 (1981).
- [50] G.R. Luckhurst, *Mol. Phys.* **82**, 1063 (1994).
- [51] The definition of the nearest neighbors is based on the Voronoi construction, which assigns a Voronoi cell to each molecule, defined (in two dimensions) as the region of the plane that is closer to a given molecule than to any other molecule. Any pair of molecules whose Voronoi cells share a side are taken to

- be nearest neighbors. See, for example, J.P. McTague, D. Frenkel, and M.P. Allen, in *Ordering in Two Dimensions*, edited by S.K. Sinha (North-Holland, Amsterdam, 1980).
- [52] M. Hara, H. Takezoe, and A. Fukuda, *Jpn. J. Appl. Phys., Part 1* **25**, 1756 (1986).
- [53] W.G. Jang, M.A. Glaser, C.S. Park, K.H. Kim, Y. Lansac, and N.A. Clark (unpublished).
- [54] While induction interactions are not treated explicitly in this simulation, they are included implicitly in an approximate way via effective van der Waals interaction parameters. These parameters are determined empirically, as described in the Appendix. Our results suggest that this is a reasonable first approximation, provided that the thermodynamic conditions of the simulation do not differ significantly from those for which the empirical determination of van der Waals interactions was carried out.
- [55] W.L. Jorgensen, J.D. Madura, and C.J. Swenson, *J. Am. Chem. Soc.* **106**, 6638 (1984); J.M. Briggs, T. Matsui, and W.L. Jorgensen, *J. Comput. Chem.* **11**, 958 (1990); W.L. Jorgensen, E.R. Laird, T.B. Nguyen, and J. Tirado-Rives, *ibid.* **14**, 206 (1993); J.M. Briggs, T.B. Nguyen, and W.L. Jorgensen, *J. Phys. Chem.* **95**, 3315 (1991).
- [56] GAUSSIAN 94, Revision D.4, M.J. Frisch, G.W. Trucks, H.B. Schlegel, P.M.W. Gill, B.G. Johnson, M.A. Robb, J.R. Cheeseman, T. Keith, G.A. Petersson, J.A. Montgomery, K. Raghavachari, M.A. Al-Laham, V.G. Zakrzewski, J.V. Ortiz, J.B. Foresman, J. Cioslowski, B.B. Stefanov, A. Nanayakkara, M. Challacombe, C.Y. Peng, P.Y. Ayala, W. Chen, M.W. Wong, J.L. Andres, E.S. Replogle, R. Gomperts, R.L. Martin, D.J. Fox, J.S. Binkley, D.J. Defrees, J. Baker, J.P. Stewart, M. Head-Gordon, C. Gonzalez, and J.A. Pople (GAUSSIAN, Inc., Pittsburgh, PA, 1995).
- [57] C.M. Breneman and K.B. Wiberg, *J. Comput. Chem.* **11**, 361 (1990).